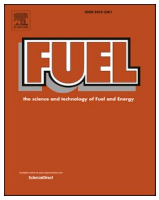
Fuel 381 (2025) 133405



Contents lists available at ScienceDirect

Fuel

journal homepage: www.elsevier.com/locate/fuel



Full Length Article



Mechanical deformation destabilizing hydrate within thermodynamic equilibrium region

Peng Zhang [a,1], Xueping Chen [b,1], Rui Bao [c], Xu Ma [a], Yulu Wang [a,i], Yangli Che [c], Lianhai Zhang [a], Yingmei Wang [h], Jing Zhan [a], Guangjun Guo [e,i], Changyu Sun [f], Jianyang Wu [g], Qingbai Wu [a,*], Shuanshi Fan [d,**]

[a] Key Laboratory of Cryospheric Science and Frozen Soil Engineering, Northwest Institute of Eco-Environment and Resources, Chinese Academy of Sciences, Lanzhou 730000, China
[b] Institute of Geological Hazards Prevention, Gansu Academy of Sciences, Lanzhou 730000, China
[c] Frontiers Science Center for Deep Ocean Multispheres and Earth System, Key Laboratory of Marine Chemistry Theory and Technology of Education Ministry, Ocean University of China, Qingdao 266100, China
[d] Key Laboratory of Heat Transfer Enhancement and Energy Conservation of Education Ministry, School of Chemistry and Chemical Engineering, South China University of Technology, Guangzhou 510640, China
[e] Key Laboratory of Petroleum Resource Research, Institute of Geology and Geophysics, Chinese Academy of Sciences, Beijing 100029, China
[f] State Key Laboratory of Heavy Oil Processing, China University of Petroleum, Beijing 102249, China
[g] Department of Physics, Research Institute for Biomimetics and Soft Matter, Jiujiang Research Institute and Fujian Provincial Key Laboratory for Soft Functional Materials Research, Xiamen University, Xiamen 361005, China
[h] Western Energy & Environment Research Center of China, Lanzhou University of Technology, Lanzhou 730050, China
[i] University of Chinese Academy of Sciences, Beijing 100049, China

ARTICLE INFO

Keywords:
Natural gas hydrates
Mechanical deformation
Piston-like accelerator
Destability

ABSTRACT

Natural gas hydrates are a significant potential energy source and key player in global geological climate dynamics, with our all understandings on both sides basing on hydrate stability conditions consisting of pressure (P) and temperature (T). Considering important significance of theoretical researches in two sides, whether there is another factor playing same role with P or T is worth being answered. Using molecular dynamics simulations, changes of non-clathrated water structures and gas bubbles during mechanical deformation processes of methane hydrates were investigated to characterize their destabilizing natures and the deformation is then identified as this new factor. Similar to P-T profile but at a new level of complexity, deformation also characterizes hydrates stability but in three-dimensional space form while combining with T, reflecting deeper influences of specific temperature values, hydrate purities and deformation modes on hydrates stability. Over two tensile and compressive deformations, the mechanisms responsible for hydrate destabilization vary, with stretching favoring formation of gas bubbles and compressing damaging internal hydrogen-bond structures. Once alternating, such two to-and-fro continuing deformations can act as a piston-like accelerator as well as one-way valve for dissociation of hydrates, destabilizing them rapidly. In summary, P and T act as the prerequisite of hydrate existences, but cannot accurately account for the influence of such dynamic events as earthquakes, ocean tides, and changes of ice shelves on dissociations. This research sheds a new light on the reasonable explanation to dynamic hydrate dissociations, e.g. some abnormal disappearances of reservoirs within appropriate P-T conditions. Stronger, current bottleneck of hydrate exploitation efficiency might also be broken down; likewise, the ultra-rapid dissociation performance during the terminal procedure of hydrate-based natural gas storage/transportation technology might achieve success.

* Corresponding author at: Key Laboratory of Cryospheric Science and Frozen Soil Engineering, Northwest Institute of Eco-Environment and Resources, Chinese Academy of Sciences, Lanzhou 730000, China.
** Corresponding author at: Key Laboratory of Heat Transfer Enhancement and Energy Conservation of Education Ministry, School of Chemistry and Chemical Engineering, South China University of Technology, Guangzhou 510640, China.
E-mail addresses: qbwu@lzb.ac.cn (Q. Wu), ssfan@scut.edu.cn (S. Fan).
[1] P. Zhang and X.P. Chen contributed equally to this work.

https://doi.org/10.1016/j.fuel.2024.133405
Received 21 July 2024; Received in revised form 23 September 2024; Accepted 8 October 2024
Available online 19 October 2024
0016-2361/© 2024 Elsevier Ltd. All rights are reserved, including those for text and data mining, AI training, and similar technologies.

1. Introduction

Natural gas hydrates, one type of non-stoichiometric compounds of hydrogen-bonding polyhedral water cavities with gas molecules trapped inside [1], have been a scientific curiosity since last century. Owing to the common findings in natural environments [2], they have attracted significant attention to the ability of trapping energy- and environment-related gases such as methane and carbon dioxide [3]. Research on hydrates has expanded to include important issues like climate change, energy recovery [4,5], and gas storage/transportation [6,7].

One of most studied scenarios is the potential destabilization of hydrate deposits in ocean due to warming climate [8–10], which could lead to release of methane into the atmosphere, exacerbating greenhouse effect and further destabilizing hydrates. Past events like significant global warming during the Late Quaternary period [11] and Paleocene-Eocene Thermal Maximum [12] have been linked to hydrate degradation. On present basical theory, hydrates stability is determined by elevated pressure (P) and low temperature (T) (Fig. 1) [13]. A common method to obtain exact P-T conditions of hydrate phase equilibrium is through measuring the intersection points in cooling and heating isochor curves during formation and dissociation processes [14]. The research on natural gas hydrates began around 90 years ago when they were discovered blocking gas transmission lines in Canada [15]; thereafter, natural samples were recovered in the Black Sea [16]. Since then, numerous studies worldwide have focused on basical researches on hydrate equilibrium P-T conditions [13,17], using experiments, models, and simulations.

Due to warming ocean waters [18] and deglaciation effects [19], it is speculated that the hydrates in certain geological settings, especially at high northern latitudes, may already break down. While some methane released from the seafloor has reached atmosphere [20], the methane fluxes observed at high-latitude sites cannot be directly attributed to hydrate degradation [21]. It is generally agreed within the academic community that catastrophic gas releases from hydrates due to warming would take centuries or even millennia, suggesting that present-day natural gas hydrates are currently stable [8]. However, some researchers also suggest that hydrates should be viewed as dynamic systems with carbon fluxes from ocean [22]. For example, hydrates beneath ice sheets in Antarctica [23] and Greenland [24] could be affected by deglaciation and lead to future methane releases. Despite this, there is still a lack of understanding of how hydrates are destabilized dynamically by some factor other than P and T (Fig. 1). A recent research finding on gas emissions in the Arctic water column suggest that methane emissions may be linked to tectonic stress fields and strains, caused by periodic tides [25]. During the low tide cycles, hydrostatic pressure reduction may cause the gas pressure (P_g) within pre-existing gas hydrate reservoirs to exceed the pressure threshold needed to generate tectonic micro-deformation. During high ones, the system will be under a balanced pressure field where minimum principal stress and strength of hydrate patches are enough to counteract P_g within system [25]. And a little 4 kPa deviation of hydrostatic pressure is enough to decrease the effective stress below a pressure threshold corresponding to tensile strength of sediments and to generate gas release [26]. In addition, molecular-scale simulations have shown that the strain-induced dissociation of methane hydrate polycrystals can occur even within the thermodynamic stability region [27]. Taken together, such coincidental consistency between macro- and micro-scale conclusions suggests that besides P and T, mechanical strain may play a significant role in hydrate stability.

Traditional method of determining hydrate stability conditions [14], which focuses on the disappearance of infinitesimal amounts of hydrate crystals, provides insights into the microscopic dynamic processes that underlie macroscopic thermodynamic observations. The measurements of strain-induced dissociation should therefore also involve infinitesimal amounts of hydrate crystals and Molecular Dynamics (MD) simulations [27,28] appearing as a reasonable approach. To shed new light on destabilization of methane hydrates under mechanical stress and strain, different P-T conditions and gas encapsulation efficiencies, the software LAMMPS (Large-scale Atomic/Molecular Massively Parallel Simulator) was chosen and utilized.

2. Methodology

2.1. Molecular modeling

Establishment procedure of methane hydrate unit cell is as follows (Fig. 2). In the light of X-ray diffraction analysis of ethylene oxide hydrate, initial coordinates of oxygen atoms were obtained; and methane molecules were then placed in the central position of water cages and occupied 100 %. And after initial hydrogen atoms of water molecules were allocated randomly, the network structure with lowest energy hydrogen bonds was generated by Monte Carlo method following the Bernal-Fowler criterion. After that, methane hydrate crystal structures were established. Firstly, the monocrystalline hydrate structure was established as follows. Replicating above unit cell by 20 × 20 × 20 times, hydrate super crystalline cell with size 23.24 × 23.24 × 23.24 nm^3 was constructed, with 432,000 atoms contained. To reveal the effect of crystal orientation on production of non-clathrated water structures, other orthogonal structures were obtained by processing the cubic single crystal structure. Monocrystalline hydrate structures along crystal

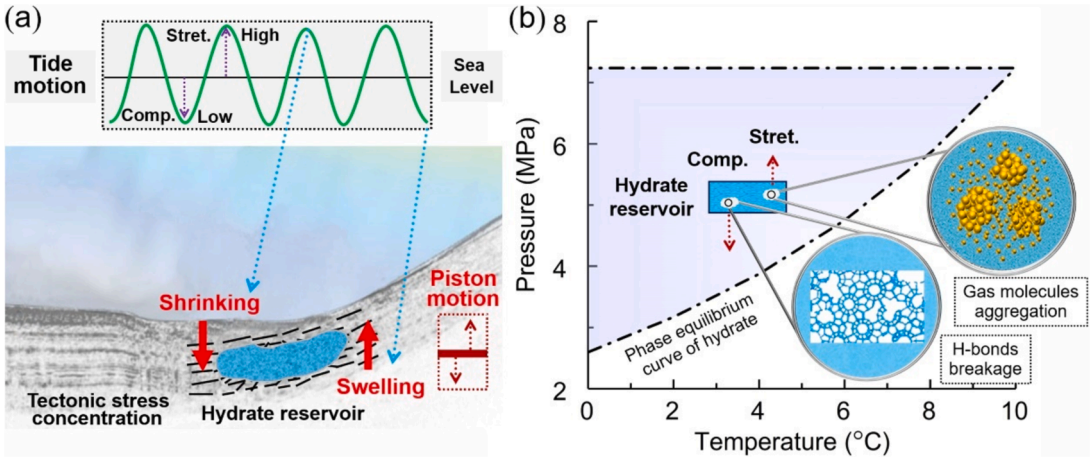


Fig. 1. Schematic of dynamic piston-like accelerator for hydrate destability within thermodynamic phase equilibrium region. (a) hydrate reservoir under seafloor, (b) destability mechanism.

direction of [1 1 0] and [1 1 1] respectively had three-dimensional dimensions of 232.40 × 230.06 × 230.06 Å^3 and 227.70 × 230.06 × 241.51 Å^3, with 423, 360 and 435, 456 atomic numbers. With the conjugate gradient method [29], finally established structure was quasi-statically relaxed to local energy minimization, by limiting energy and force convergences to 1.0 × 10^{-4} eV and 1.0 × 10^{-4} eV/A. After enough relaxation, a reasonable molecular configuration was obtained. And basing above single-crystal hydrate unit cell, a polycrystal model of hydrates with 9 grain numbers was constructed using Voronoi tessellation method. Firstly, random numbers, i.e. space points, in a body-centered cubic arrangement were selected; secondly, the hydrate unit cell was copied and rotated around them and then truncated into octahedron to generate some single grains; subsequently, these single grains were randomly assembled into polycrystals. Finally, nine kinds of polycrystalline hydrates with grain numbers 54, 128, 250, 432, 686, 1024, 1458, 2000, 2662 and all sizes 23.24 × 23.24 × 23.24 nm^3 were constructed. Using same energy minimization method as that for the monocrystalline, reasonable configurations of polycrystalline hydrates were obtained.

After that, force fields were set. In order to describe hydrate and water molecules contained in both monocrystalline and polycrystalline hydrates, a mono-atomic model was utilized. The tetrahedral short-ranged interactions among mono-atomic water molecules were modeled by the Stillinger-Weber (SW) model. The potential function is expressed as follows.

$$U = \sum_i \sum_{j>i} A_{ij}\varepsilon_{ij}\left[B_{ij}\left(\frac{\sigma_{ij}}{rij}\right)^{p_{ij}} - \left(\frac{\sigma_{ij}}{rij}\right)^{q_{ij}}\right] e^{\frac{\sigma_{ij}}{r_{ij}-a_{ij}\sigma_{ij}}}\Theta(a_{ij}\sigma_{ij} - r_{ij}) + \sum_i \sum_{j\neq i} \sum_{\substack{k\neq i \\ k>j}} \lambda_{ijk}\varepsilon_{ij}$$

where, r_{ij} is the distance between particles i and j, r_{ik} between i and k, and θ_{ijk} represents the angle between position vectors r_{ij} and r_{ik}. Value λ determines the strength of tetrahedral interaction. Following Table 1 displays the detailed values of molecular force field parameters for coarse-grained water and methane.

2.2. Mechanical deformation simulation

All the simulation calculations were implemented using the software package LAMMPS (Large-scale Atomic/Molecular Massively Parallel Simulator), under periodic boundary conditions and three orthogonal directions. Before exerting mechanical loadings, the structures were all relaxed respectively under NPT (constant particles numbers, pressure and temperature) and NVT (constant numbers, volume and temperature) ensembles to achieve the initial simulation conditions required by loadings. During relaxations, the T and P were maintained same as initial ones through Nosé-Hoover control technique, of which the damping control coefficients were 0.1 ps for T and 0.5 ps for P.

Using displacement control technology, mechanical loadings were exerted in the modified ensembles: for the NVT, loading was in z direction; for NPT, in two lateral x and y directions. By uniformly rescaling z coordinates of all atoms every 100 timesteps, loading procedure was performed on the interface of relaxed systems, using Nosé-Hoover method to control the T and P anisotropy. P and T along x and y directions were all controlled, with the damping coefficients of them retaining same as that during relaxation processes. Owing to Poisson's ratio effect, the utilized Nosé-Hoover T and P control method allowed transverse expansion and compression of simulated structures. Basing the definition of virial stress and forces received by each atom over dynamic process, stress of each atom was calculated. And the Newton's equation of motion was solved numerically by Velocity-Verlet algorithm. Definition of tensile or compressive strain was same as that of engineering strain. Specific expression is

$$\varepsilon = \frac{|l-l_0|}{l_0} = \frac{\Delta l}{l_0}$$

where, ε, l_0, and l signify engineering strain, initial and final lengths of simulated box.

2.3. Interpolation-supplemented Matlab calculation method

Firstly, the changes in hydrate dissociation ratios along with deformation ones under temperatures 268.15 K, 273.15 K, 278.15 K and 283.15 K were obtained, by using software Ovito. Secondly, obtained data under every temperature were divided into three sections and then fitted to three quadratic equations for obtaining excellent correlation coefficients (Excel Table S1). Finally, using the interpolation operation method, these data at an interval of 0.125 K between two nearest-neighbour temperatures were supplemented using software Matlab. Taking only the hydrate with 54 grains over stretching under four temperatures for instance, the specific operation routines are displayed in the supplementary information.

Similarly, the changes in dissociation ratios along with deformation ones for hydrates with different grains under four temperatures were obtained firstly. And the data at an interval of 0.1 between two nearest-

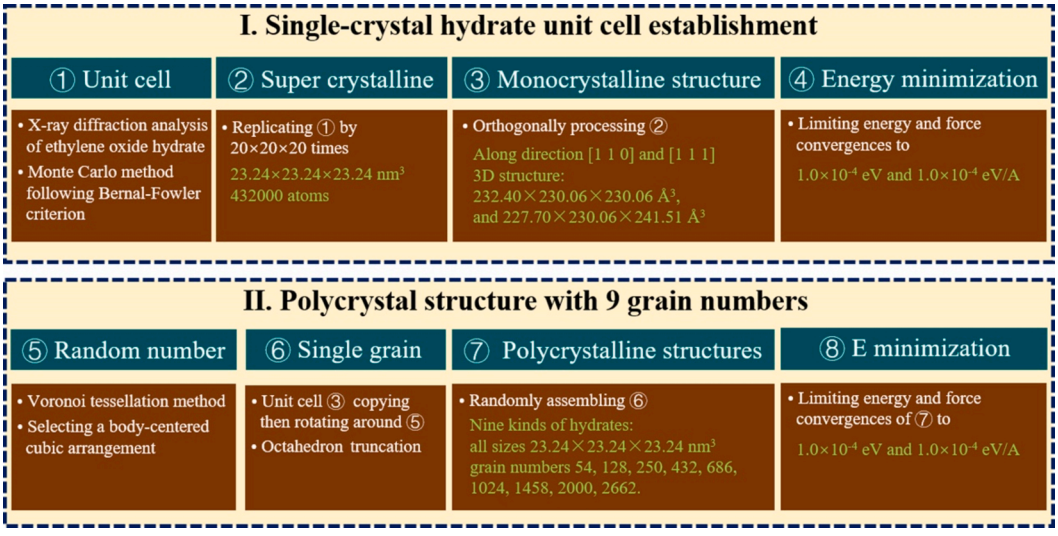


Fig. 2. Modeling procedure for polycrystal hydrate structures with nine grain numbers.

Table 1
Detailed values of molecular force field parameters.

	E(kcal/mol)	σ (Å)	a	λ	γ	θ_0	A	B
Water-Water	6.189	2.3925	1.8	23.15	1.2	109.5°	7.049556227	0.6022245584
Water-Methane	0.34	4.08	1.8	0	1.2	–	–	–
Methan-Methan	0.18	4.00	1.8	0	1.2	–	–	–

neighbour molar ratios of water to gas at each temperature were obtained, with the interpolation-supplemented method in Matlab. The data for each hydrate at 268.15 K were also similarly divided into three sections with above same purpose (Excel Tables S2 and S3). Taking only the hydrates with all 9 grain numbers over stretching at 268.15 K for instance, specific operation routines are also exhibited in supplementary information.

3. Results and discussion

3.1. Strain-induced destabilization of hydrates with different grain numbers

The curved planes 1–9 in Fig. 3(a) and (c)–(e) respectively symbolize hydrates with grains 54, 128, 250, 432, 686, 1024, 1458, 2000 and 2662. As illustrates, the dissociation behaviors of hydrates having various grain numbers under tensile deformation ranging from 0 % to 30 % and temperatures between 268.15 K and 283.15 K (Excel Table S1). Upon stretching, all crystals exhibit a slight re-formation period instead of immediate dissociation, characterized by regions with negative dissociation ratios of approximately 0 % to –3 %. For the crystal with 54 grains (plane1), this negative ratio reaches a minimum at a deformation of 2.75 % and temperatures between 268.15 K and 269.9 K, which increases with temperature up to 3 % between 279.525 K and 283.15 K. This similar behavior is also observed in planes 2 and 3, while a reverse pattern emerges for plane 4 and above (more detailed data in Table S1). These negative dissociation ratios reflect a self-recovery capacity of hydrate crystals against strain-induced dissociation. Analyzing the minimum dissociation ratios over different stretches (Table S1), this capacity at lowest temperature 268.15 K strengthens with an increase in grain numbers up to 1458 before sharply weakening by around 7 times at 2662 grains. This suggests that increasing grain numbers within the range of 54 to 1458 enhances the self-recovery capacity under a temperature increase of approximately 3 K from lowest 268.15 K. However, for hydrates with 1024, 1458, and 2000 grains, this capacity weakens with temperatures rising. Fig. 3(b) depicts the initial cavity structures of hydrates composed of hydrogen bonds and their changes under tensile deformations, in which the hydrogen-bond structures displayed are all in (1 0 0) planes with a thickness of 10 Å. The complete clathrate structures decrease in number from around 125 to 64 and then to 1 as the grain numbers increase from 54 to 2662. The interfaces between grains play a crucial role in distinguishing these structures, with closer

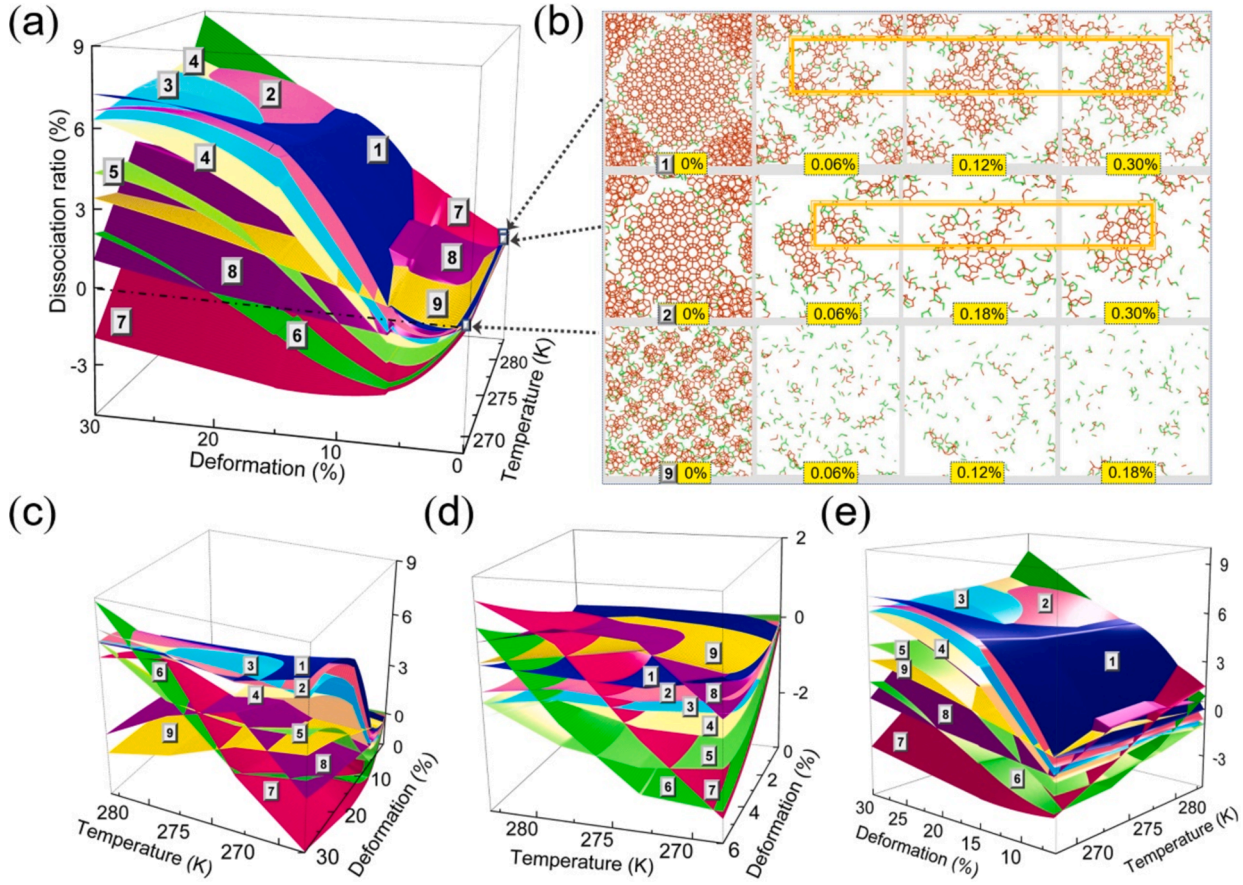


Fig. 3. Deformation dissociations and changes of hydrogen-bonded structures. (a) hydrates with grains 54, 128, 250, 432, 686, 1024, 1458, 2000 and 2662, numbered 1 ~ 9; (b) changes in hydrogen-bonds of hydrates with grains 54 at 283.15 K, 128 at 283.15 K and 2662 at 268.15 K, numbered 1, 2 and 9; (c) axially rotated (a); (d)~(e) magnified segments 0 ~ 6 % and 6 ~ 30 %.

interfaces facilitating the insertion of interfacial bonds into complete clathrate structures. The recovery of damaged clathrate structures during stretching is evident, particularly for lower grain numbers (Figs. S1-S3), while hydrates with 2662 grains show weaker recovery behavior. During deformation of 0 ~ 10 %, the curved planes exhibit an obvious strain tolerance stage of hydrate crystals and distinct varying patterns, with planes 1–6 showing similar variations and 7–9 displaying contrasting patterns as follows. The latter planes tend to become flat (Fig. 3 (d) and (e)) and cover the others during deformation up to 9.5 % (Fig. 3 (e)). With increasing temperature, the uncovered segments of planes 7–9 rise in a stepped pattern (Fig. 3(a) and (e); Figs. S4-S7). Similar stepped patterns are observed for planes 1–4, not only with temperature rise but also with increase of deformation ratio (Fig. 3(a)).

After the strain tolerance stage, hydrates lose their self-recovery capacity and begin to dissociate, with dissociation behavior influenced also by grain numbers and temperature. Dissociation degrees between deformations of 9.5 % to 16 % are dependent on grain numbers. For planes 1 to 7, higher grain numbers of hydrate correspond to lower dissociation ratios, while planes 8 and 9 show opposite pattern, resulting in multiple intersections between the two groups (Fig. 3(a)). Beyond a 16 % deformation, dissociation ratio of hydrate symbolized by plane 1 gradually decreases with increasing deformation and temperature. Due to higher dissociation ratios, plane 3 exhibits the highest dissociation ratio followed by plane 2, along the boundary line between deformations of approximately 19.5 % at 273 K and 26.75 % at 278 K. Along the boundary between deformations of 27.25 % at 279 K and 29.75 % at 279 K, plane 4 shows the highest dissociation ratio. This results in a stepped pattern of variation for planes 1 to 4. Additionally, after the minimum dissociation ratios, the separation distance between planes 1 to 7 tends to increase with rising deformation. Using the distance between planes 1 and 2 as a reference, the distances between these parallel planes (1 to 7) increase by times of approximately 1.4, 1.9, 2.9, 5.1, and 6.8 sequentially. This indicates that hydrates with smaller grain numbers are more easily dissociated by deformations, while planes 7 to 9 show a reverse pattern of variation.

During all stretching simulations, confining pressures maintained at a uniform 10 MPa. However, all hydrate crystals with nine types of grains were destabilized as they stretched, even within thermodynamic phase equilibrium regions. Unlike the two-dimensional P-T phase equilibrium diagram [13], the strain-induced dissociation diagram is significantly more complex in three dimensions, showing relationships with intrinsic and external factors of hydrates such as grain numbers, temperature, and deformation amplitude. Upon stretching initiation, the hydrates do not immediately dissociate but undergo a re-formation process before dissociation, indicating a self-recovery capacity of hydrate structures against deformation. And this capacity closely relates to grain number and temperature conditions.

The numbers of grains mentioned above represent different hydration levels of hydrates formed during simulations, as well as the ratios of gas contained in the hydrates (Table S2) and amounts of non-clathrated water structures [30], also known as the aqueous quasi-liquid layer (QLL) [31] existing at grain interfaces. These strain-induced dissociations are significantly different from the phase equilibrium profile based on P and T [13], as they are directly influenced by specific temperatures and gas ratios within hydrates. When considering the heterogeneity, regionality, and locality of hydrates [32–34], it becomes clear that predicting hydrate destabilization based solely on P and T is insufficient. After combining with temperature, mechanical deformation can characterize hydrates destability in a 3D form (Fig. 3(a)), complementing above shortcoming and allowing for the prediction of potential hydrates dissociations in nature within global P-T conditions [35,36]. Accordingly, the variations in locations of hydrate reservoirs can be explained with diversity of gas sources and environmental conditions globally.

The strain-induced destabilization profile of hydrates (Fig. 3) also reflects a dynamic feature that enhances the understanding of thermodynamic P-T equilibrium profile and complements the theory of dynamic processes [22] not involved in P-T profile. These dynamic destabilization processes are closely linked to the presence of significant amounts of non-clathrated water structures [30], between hydrate grain interfaces, which provide a buffering function against strain-induced dissociation. In summary, this research sheds a new light on these areas beyond phase equilibrium P-T profiles of hydrates.

3.2. Appearance characteristics of gas bubbles over deformations

Using the statistics on methane bubbles generated during stretches, deformation-induced dissociaiton behaviors of hydrates were further identified. As shown in Fig. 4(a), physical natures of bubbles also relate with many influencing factors, including deformation degrees, temperature, grain numbers (Figs. S8-S10), for more detailed data see Tables S3-S8. Among them, grain numbers exert greatest influence on regardless of numbers or areas of bubbles: at deformation ratio 6 %, average of bubble numbers inside hydrate with 2662 grains is larger than those with 54 and 686 ones respectively by 2.5 and 9.1 times and that of area is by 1.2 and 2.0 times; at ratio 12 %, 3.5 and 9.8, 1.2 and 2.4; 18 %, 4.4 and 9, 1.5 and 3.4; 24 %, 6.6 and 11.7, 1.6 and 3.5; 30 %, 5.6 and 8.1, 2.0 and 5.2 (Table S3). Under same grain number, temperature rise tends to elevate numbers and areas of bubbles: for instance, for the grains 686 at deformation 6 %, bubble numbers appear as 4, 12, 13, 19 respectively at 268.15 K, 273.15 K, 278.15 K, 283.15 K with average areas of 215.8 $Å^2$, 189.1 $Å^2$, 170.2 $Å^2$, 192.9 $Å^2$; and at 18 %, 5, 13, 15, 29 with that of 234.0 $Å^2$, 257.7 $Å^2$, 285.5 $Å^2$, 301.9 $Å^2$ (Excel Table S2). With larger deformation, this pattern appears more obvious (Tables S3-S8). This varying pattern is also followed by the area distributions: the differences between the maximum and minimum of average areas of bubbles under four temperatures within hydrates having 686 grains are: 188.1 $Å^2$, 212.9 $Å^2$, 225.1 $Å^2$, 287.0 $Å^2$, for deformation 6 %; 158.7 $Å^2$, 209.1 $Å^2$, 287.8 $Å^2$, 440.7 $Å^2$, for 12 %; 266.5 $Å^2$, 368.0 $Å^2$, 437.1 $Å^2$, 1457.0 $Å^2$, for 18 %; 329.5 $Å^2$, 574.5 $Å^2$, 564.3 $Å^2$, 1670.0 $Å^2$, for 24 %; and 318.0 $Å^2$, 884.0 $Å^2$, 804.6 $Å^2$, 1460.7 $Å^2$, for 30 %. This pattern is also followed by the grains 2662 (Excel Table S2); however, not suitable in one special case of grains 54 at deformation 30 % under four temperatures. Considering the gradual rising trend of each column symbolizing bubble areas in Fig. 4(a), relations between the increased percentage of each bubble area with respect to that in the minimum value and each bubble area itself for every column of Fig. 4(a) were statisticized (Table S4). In combination of the fitted quadratic equations (Table S4) and curves (Excel Table S3) for above relations, it is summarized that for generations of gas bubbles during strain-induced dissociaitons, while both temperature and grain numbers exert influences, the latter appears greater. For instance, under four temperatures, the a-values of all quadratic equations for grains 54 are of almost the same order of magnitude while undergoing five deformation ratios. By contrast, these a-values for grains 2662 elevates by 1 ~ 2 orders of magnitudes under the same conditions: along with increase of deformation ratios under each temperature, the specific magnitudes rise sharply, e.g. by 12, 10, 32.5, 43.3, 76.7 times respectively for the five deformation ratios 6 %, 12 %, 18 %, 24 % and 30 % at 278.15 K (Table S4). On the other hand, bubbles circularities in Fig. 4(a) present significantly greater temperature-dependence: e.g. the averages 0.63, 0.65, 0.69 for the three grains 54, 686, 2662 during five deformation ratios at 268.15 K, and 0.73, 0.73, 0.78 at 278.15 K, increased by 1.03 and 1.10 times, and 1.00 and 1.07 times; and 0.63, 0.65, 0.73, 0.82 for grains 54 under four temperatures and 0.69, 0.72, 0.78, 0.80 for 2662 grains, increased by 1.03, 1.16, 1.31 times and 1.04, 1.13, 1.17 times (Table S5).

Stronger, both tensile and compressive deformations also can affect the natures of bubbles. As for five the tensile deformation ratios, averages of bubble areas under four temperatures corresponding to grains 54, 686 and 2662 are: for 6 %, 153.8 $Å^2$, 192.0 $Å^2$, 314.5 $Å^2$; for 12 %, 174.3 $Å^2$, 217.1 $Å^2$, 415.6 $Å^2$; for 18 %, 176.9 $Å^2$, 269.8 $Å^2$, 595.0 $Å^2$; for 24 %, 208.5 $Å^2$, 340.3 $Å^2$, 738.5 $Å^2$; and for 30 %, 163.3 $Å^2$, 330.4 $Å^2$,

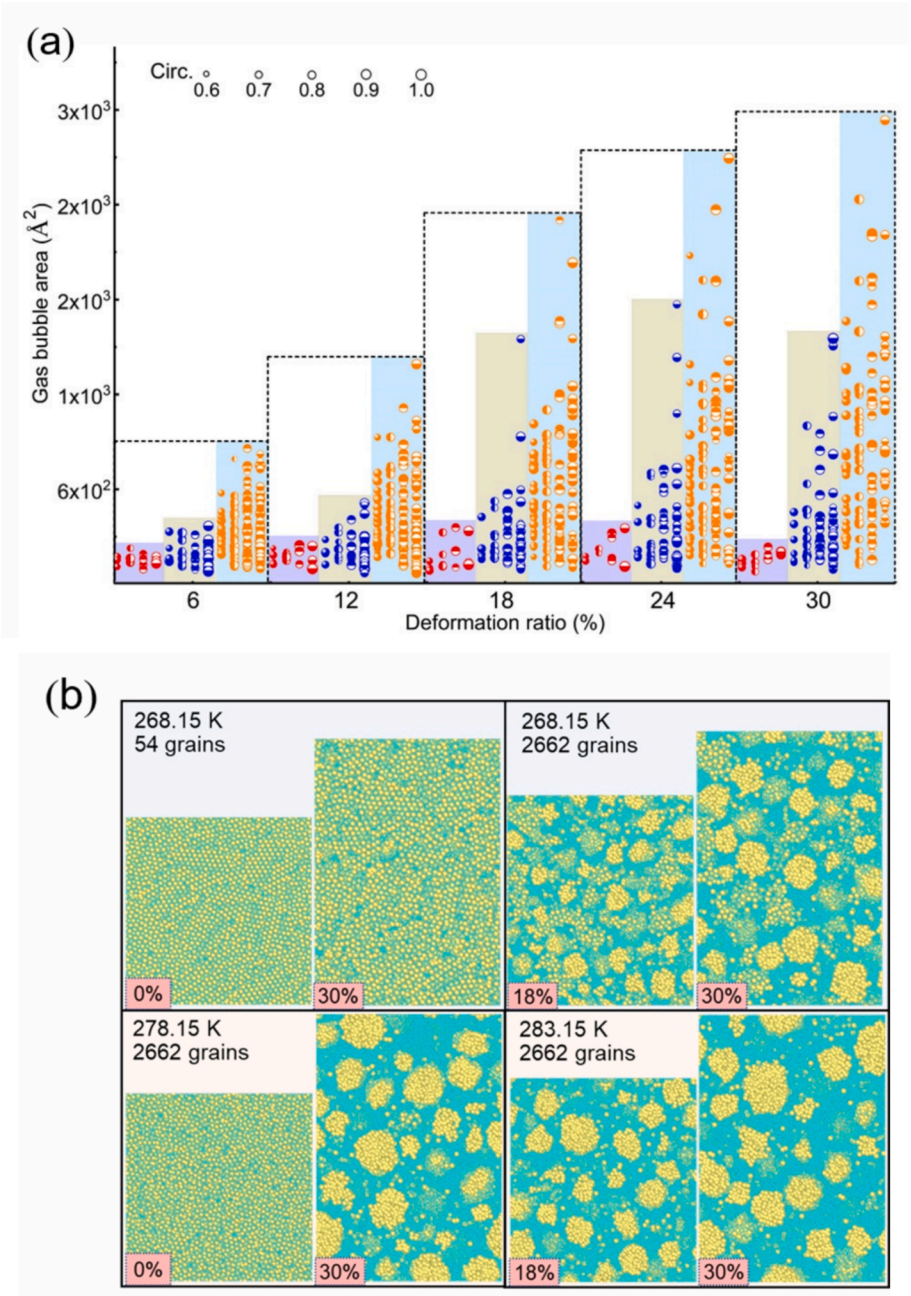


Fig. 4. Statistical results on physical parameters and appearance morphologies of bubbles generated during dissociation. (a) physical parameters with solid, right-, bottom-, top-hollow balls denoting 268.15, 273.15, 278.15, 283.15 K, and light purple, dark yellow and cyan backgrounds denoting hydrates with grains 54, 686, 2662; (b) bubble morphologies in (1 0 0) plane intercepted. (For interpretation of the references to colour in this figure legend, the reader is referred to the web version of this article.)

849.6 Å^2 (Fig. 4(a) and Excel Table S2). These contrasting averages under compress ratios are lowered respectively as follows (Fig. S11): by −10.2 %, −7.9 %, 1.1 %; 2.8 %, −16.8 %, 4.2 %; 30.9 %, 0.2 %, 11.6 %; 48.4 %, 17.4 %, 13.2 %; and 46.8 %, −4.8 %, 9.5 %. In combination of Fig. 4 and Fig. S11, the varying pattern for bubble areas tends to decrease generally with compress ratios increasing, and so also the bubble numbers (Tables S3 and S7). Comparing five stretch ratios, the varying tendency of circularities during compress ones is lowered respectively: for 6 %, by 2.5 %, 9.2 %, 0.2 %; for 12 %, 5.7 %, 2.6 %, 1.0 %; for 18 %, 1.2 %, 2.9 %, −1.2 %; for 24 %, −7.6 %, −0.6 %, −0.5 %; for 30 %, 14.4 %, −0.6 %, −0.8 % (Tables S5 and S8). This means merely over two compress ratios 24 % and 30 %, circularities tend to increase but within light amplitudes; over other residual three ones, overall decrease significantly.

Similar to generations of methane gas confirmed during the stress-induced coal dissociation [37,38], deformation-induced destabilization of hydrates is further validated through generations of gas bubbles (Fig. 4(b), Movies S1-S16), with larger deformaitons generally resulting in severer dissociation but other than one special case of grains 54. This implies very high hydrate purity can resist such kind of dissociations, especially for the drastic deformation ratio of 30 %. Numbers and areas of bubbles generally elevate along with deformation increase, with closely relating to specific temperature under which hydrates exist and encapsulation efficiencies of gas molecules (Table S2). In addition to some fitted quadratic equations (Table S4), it is summarized that while containing more great amount of non-clathrated water structures inside,

hydrates provide more appropriate intrinsic condition for generation of gas bubbles with greater numbers and area sizes. This means that during deformations, lower purity, i.e. greater grain number, is detrimental to hydrate stability. Higher temperature as well as greater grain number can more deeply enhance circularities of bubbles. Given that more circular bubbles signify lower free energy of system and higher bubbles stability, it is almost impossible for such damaged hydrate stability by higher temperature to be recovered, with a logical reason of that the lower free energy facilitates gas bubbles to generate deeper potential wells trapping surrounding gas molecules. Therefore, once generating, these methane molecules will be sucked away from surfaces of broken hydrate structures and adsorbed on those of as-formed bubbles easily, under the transport function of concentration gradients [39].

In summary, a considerable amount of non-clathrated water structures existing between hydrate grains facilitates the precipitation environment of gas bubbles inside hydrate, by reducing the free energy of global bubble system [3]. And higher temperature under which hydate exists provides essential driving force of bubbles growth and stability, allowing for a reasonable explanation to why higher temperature is detrimental to hydrate stability.

3.3. Influence of deformation types on hydrate destability

Fig. 5 displays that despite generally similar appearances of curved planes reprsenting dissociation behaviors, specific dissociation ratios induced by compresses are significantly higher than those by stretches under same temperature (Figs. S1-S7 and Figs. S11-S15). For example, the deviation between planes i and ii at 268.15 K and the highest 92.3 % purity in Fig. 3(a) becomes larger gradually, i.e. for the hyrate with 54 grains, deviations of dissociaiton ratios between two deformation types rise from 0.05 % to 7.24 % with deformation amounts from 0 % to 30 %. By contrast, those for 2662 grains also at 268.15 K but lowest 17.6 % purity are just from −0.07 % to −0.3 %. Also for these two same grains, the deviations respectively at highest and lowest purities under different temperatures are: at 273.15 K, from −0.01 % to 7.48 % and from −0.01 % to 0.14 %; at 283.15 K, from −0.01 % to 5.83 % and from 0.09 % to 0.39 % (Fig. 5 and Fig. S14). Along with initial hydrate purity lowering, i.e. grain number increasing, these deviations disappear grudually, with two curved planes merging together along these boundary lines for purities of approximately 40 % at 268.15 K, 29 % at 273.15 K, 25 % at 278.15 K and 32 % at 283.15 K. In addition, merely for the stretches, there is a threshold line of 86 % purity to distinguish the monotonic or not influence of temperature on dissociation ratios over complete deformation of from 0 % to 30 % (Fig. 5(b)); for the compresses, that line is 78 %.

Above patterns imply the greater damages of compresses to hydrate destability, with a possible main reason of that comparing stretching, the interior clathrate structures can be invaded and damaged more easily by the interfacial quasi-liquid layer structures [40] between hydrate grains over compressing. In addition to the more intense facilitation of gas bubbles to dissociation by sucking away gas molecules from surfaces of broken-down grains and then adsorbing them on those of as-formed bubbles, significant deviations between two deformations are observed.

3.4. Damage of deformations to hydrogen-bond structures

Fig. 6, also Figs. S16-S18, depict the changes of hydrogen-bond angle and length structures over deformations at 273.15 K. At 0 % deformation, the initially constructed crystal structures appear as pointed peak profiles and then collapse once deformation beginning. Most of plotted contour lines, symbolizing amounts of hydrogen-bond angle and length, retain horizontal and parallel to each other, with a meaning of the structures nondamaged. Therefore, only these closed and (or) the first non-closed curves on crestal positions of curved surfaces have analyzing meaning to damages of hydrogen-bond structures. For the hydrate with 54 grains during stretch ratios of 0 % to 30 %, the amounts of contour lines denoting angles decrease from 23 to 20, and for the 686 grains, from 25 to 22; over compress ones, respectively 23 to 17 and 25 to 19. This means inside two hydrates, 13 % and 12 % respectively of angle structures (Fig. 6(a) and (b)) are damaged and then disappeared by stretching, and 26 % and 24 % by the compressing (Fig. S16A, B). The amounts of bond lengths disappeared by two deformations are two 10 % (Fig. 6(e) and (f)) and two 20 % (Fig. S16E and F) respectively for above two hydrates. For inside 1458 grains, the angle disappearance ratios over two deformations are 7 % and 8 % and length ones are 0 % and 17 %, reflecting a positive influence of initial purities on structure damages. Inside hydrate with 2662 grains, two structures disappear after two complete deformations.

Considering greater amounts of bond angles than that of lengths, which are displayed by the specific interval values between two nearest-neighbour contours in Fig. 6, it is observed that under compresses, the destability of hydrates with higher purities (e.g. 54 and 686 grains) attribute mostly to bond-angle damages; otherwise, to bond-length ones (e.g. 1458 and 2662 grains). As the deviations of damages to clathrate structures between two deformations appears weak gradually with decrease of initial hydrate purities, these all curved planes symbolizing two deformations in Fig. 3(a) tend to merge together while purity is beneath approximately 40 %. This might also relate with the increase of the non-clathrated water structures existing between hydrate grains,

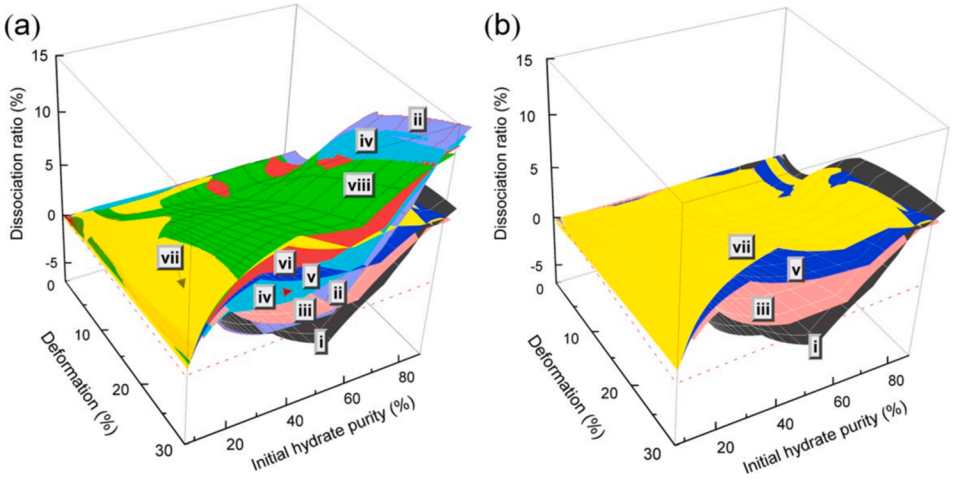


Fig. 5. Comparison of dissociation patterns of hydrates having different initial purities under same four temperatures as in Fig. 3(a). (a) both tensile and compressive deformations, (b) merely the tensile.

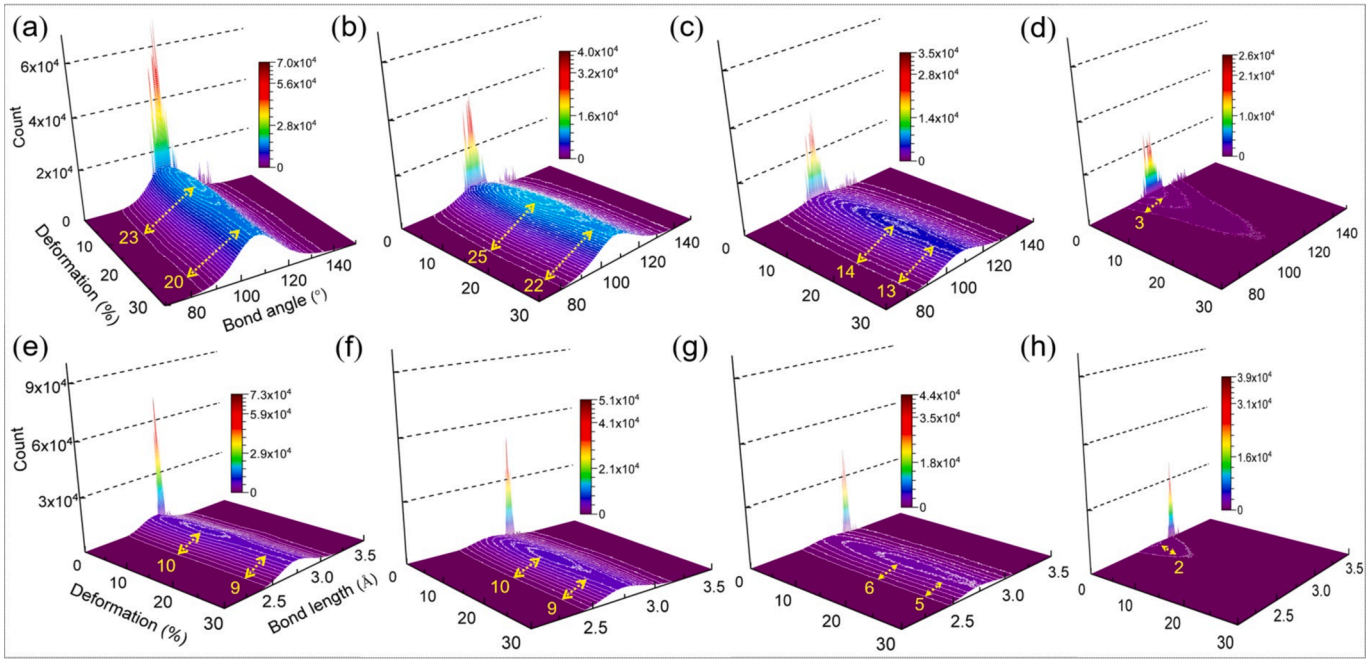


Fig. 6. Curved planes with contour lines for count changes of hydrogen-bond angle and length over tensile deformations under 273.15 K. (a)~(d) angle changes of hydrates having grains 54, 686, 1458, 2662, with intervals between two nearest-neighbour contours of 700, 398, 352, 261; (e)~(f) length changes of same hydrates, with intervals 732, 514, 438, 392.

which appear quitely similar to liquid water with amorphous structure of stretchability and incompressibility [40–42].

3.5. *Effect of deformation while combining with temperature on hydrate stability*

As discussed above, over complete compressive processes, the damages to clathrate structures of hydrates with higher (e.g. 54 and 686 grains) and lower (e.g. 1458 and 2662 grains) purities mostly ascribe to hydrogen-bond angle and length collapses respectively. Whereas, over stretches, the number, area, circularity and agglomeration environment of gas bubbles facilitate hydrate destability more effectively than over the compressings, with generated gas molecules being easily sucked away from surfaces of broken grains and then adsorbed on those of as-formed bubbles. Considering such significant diversity between specific dissociaiton processes and mechanical deformation types, it is logically deduced that upon alternating, such two to-and-fro continuous deformations act as a piston-like accelerator for hydrates destability (Fig. 1). In addition to generation of gas bubbles, this accelerator also further acts as a one-way valve of hydrate destability through lowering gas concentrations [43–45], implying the cumulativity and non-recoverability of hydrate dissociation once being induced by deformations.

As the transmission manner between mechanical stress and thermodynamic pressure is quite different, Fig. 1 further implies that once occurring within some tectonic stress concentration regions, such macroscopic stress-transmitting events as earthquakes, retreats of ice-shelf and ocean tides especially beneath the ice sheets in Antarctica [23] and Greenland [24] possess very high possiblity to induce these to-and-fro continuous deformations. Then, such hydrate reserviors under-seafloor even within thermodynamic stability region would destabilise acceleratedly.

4. Conclusion

Despite belonging to mechanical but not thermodynamic category, tensile and compressive deformations can also play same role as the thermodynamic P and T in destabilizing gas hydrates. From this, some main conclusions are summarized as follows: (1) Mechanical deformation is confirmed as a factor with an equivalent role to pressure and temperature, significantly affecting the stability of hydrates. By combining with T, it can characterize hydrate stability in a form of 3D space. (2) This 3D form reflects the deeper influences of specific temperature values, hydrate purities, and deformation modes on stability, which is incapable for the 2D P-T profile. (3) Different mechanisms are responsible for hydrate destabilization under two deformations.The tensile favors formation of gas bubbles, while the compressive damages internal hydrogen-bond structures. (4) Alternating tensile and compressive deformations can act as a piston-like accelerator and one-way valve for hydrate dissociation, acceleratedly destabilizing the hydrates.

Although having a higher level of complexity, the 3D form enhances the understanding on P-T equilibrium profile of hydrates, sheds a new light on the non-covered mechanisms beyond the profile and then offer a theoretical approach to explaining the dynamic processes of hydrate dissociation. Accordingly, some abnormal disappearances of hydrate reservoirs under appropriate P-T conditions and even without the function from fluid mobilization [46], or gas seepage [2] seems quite logical, e.g. the disappearances under dynamic events as earthquakes, ocean tides, and changes of ice shelves. And the current bottleneck of hydrates exploitation efficiency dependent on P-T profile might also be broken down using such 3D form. For instance, reiterative and continuous mechanical loading exerting on some local regions under seafloor can accelerate hydrate destability and release methane gas, especially for these fracture-type hydrate reservoirs. Likewise, the ultra-rapid dissociation during the terminal procedure of hydrate-based natural gas storage/transportation technology performance would achieve success, also by using external mechanical loadings to accelerate dissociation of as-formed hydrates.

CRediT authorship contribution statement

Peng Zhang: Writing – review & editing, Writing – original draft, Project administration, Methodology, Investigation. **Xueping Chen:**

Software, Investigation, Data curation. **Rui Bao:** Writing – original draft, Investigation. **Xu Ma:** Data curation. **Yulu Wang:** Data curation. **Yangli Che:** Visualization. **Lianhai Zhang:** Investigation. **Yingmei Wang:** Investigation. **Jing Zhan:** Methodology, Investigation. **Guangjun Guo:** Software, Investigation. **Changyu Sun:** Validation, Investigation. **Jianyang Wu:** Software, Investigation. **Qingbai Wu:** Visualization, Supervision. **Shuanshi Fan:** Validation, Supervision.

Declaration of competing interest

The authors declare that they have no known competing financial interests or personal relationships that could have appeared to influence the work reported in this paper.

Acknowledgements

This research is supported by the Gansu Province Science and Technology Major Special Projects (Grant No. 22ZD6FA004 to P.Z.), General Project of National Natural Science Foundation of China (No. 42276230 to J.Z.), Innovation Fund for Small and Medium-sized Enterprises in Gansu Province, China (No. 22CX3JA003 to P.Z.) and Independent Research Project of State Key Laboratory of Frozen Soil Engineering (No. SKLFSE-ZT-202103 to Z.P.). Also, all authors thankfully acknowledge the constructive suggestions on this paper provided by three anonymous reviewers.

Appendix A. Supplementary data

Supplementary data to this article can be found online at https://doi.org/10.1016/j.fuel.2024.133405.

Data availability

Data will be made available on request.

References

[1] Sloan ED. Fundamental principles and applications of natural gas hydrates. Nature 2003;426:353–9.
[2] Lu HL, Seo YT, Lee JW, et al. Complex gas hydrate from the Cascadia margin. Nature 2007;445:303–6.
[3] Hassanpouryouzband A, Joonaki E, Farahani MV, et al. Gas hydrates in sustainable chemistry. Chem Soc Rev 2020;49:5225–309.
[4] Chaturvedi KR, Sinha ASK, Nair VC, et al. Enhanced carbon dioxide sequestration by direct injection of flue gas doped with hydrogen into hydrate reservoir: possibility of natural gas production. Energy 2021;227:120521.
[5] Chaturvedi KR, Fogat M, Sharma T. Low Temperature rheological characterization of single-step silica nanofluids: an additive in refrigeration and gas hydrate drilling applications. J Petrol Sci Eng 2021;204:108742.
[6] Chaturvedi KR, Pandey A, Kumar R, et al. Role of hydrogen to promote hydrate formation of flue gas mixture of CO_2 and N_2 in silica nanofluid of single-step origin. J Environ Chem Eng 2021;9(6):106591.
[7] Chaturvedi KR, Sharma T, Trivedi J, et al. Experimental investigation for comparative effectiveness of CO_2+N_2 and CO_2+N_2+H_2 on integrated methane production and carbon storage from natural hydrate media. J Environ Chem Eng 2023;11(2):109388.
[8] Bohannon J. Weighing the climate risks of an untapped fossil fuel. Science 2008;319:1753.
[9] Mascarelli A. A sleeping giant? Nat Clim Change 2009;1:46–9.
[10] Whiteman G, Hope C, Wadhams P. Vast costs of Arctic change. Nature 2013;499:401–3.
[11] Kennett JP, Cannariato KG, Hendy IL, et al. Carbon isotopic evidence for methane hydrate instability during Quaternary interstadials. Science 2000;288:128–33.
[12] Kennett JP, Stott LD. Abrupt deep sea warming, paleoceanographic changes and benthic extinctions at the end of the Paleocene. Nature 1991;353:225–9.
[13] Koh C. Towards a fundamental understanding of natural gas hydrates. Chem Soc Rev 2002;31:157–67.
[14] Sloan ED, Koh CA. Clathrate Hydrates of the Natural Gases. 3rd ed. Boca Raton, FL: CRC Press; 2008. p. P115.
[15] Hammerschmidt EG. Formation of gas hydrates in natural gas transmission lines. Ind Eng Chem 1934;26:851–5.
[16] Yefremova AG, Zhizhchenko BP. Occurrence of crystal hydrates of gas in sediments of modern marine basins. Dokl Acad Sci, USSR, Earth Sci Sect 1975;214:219–20.
[17] Sloan ED. Clathrate hydrate measurements: microscopic, mesoscopic, and macroscopic. J Chem Thermo 2003;35:41–53.
[18] Kvenvolden KA. Methane hydrates and global climate. Global Biogeochem Cy 1988;2:221–9.
[19] Serov P, Vadakkepuliyambatta S, Mienert J, et al. Postglacial response of Arctic Ocean gas hydrates to climatic amelioration. Proc Natl Acad Sci USA 2017;114:6215–20.
[20] Andreassen K, Hubbard A, Winsborrow M, et al. Massive blow-out craters formed by hydrate-controlled methane expulsion from the Arctic seafloor. Science 2017;356:948–53.
[21] Shakhova N, Semiletov I, Leifer I, et al. Ebullition and storm-induced methane release from the East Siberian Arctic Shelf. Nat Geosci 2014;7:64–70.
[22] Dickens GR. A methane trigger for rapid warming? Science 2003;299:1017.
[23] Wadham JL, Arndt S, Tulaczyk S, et al. Potential methane reservoirs beneath Antarctica. Nature 2012;488:633–7.
[24] Lamarche-Gagnon G, Wadham JL, Lollar BS, et al. Greenland melt drives continuous export of methane from the ice-sheet bed. Nature 2019;565:73–7.
[25] Sultan N, Plaza A, Vadakkepuliyambatta S, et al. Impact of tides and sea-level on deep-sea Arctic methane emissions. Nat Commun 2020;11:5087.
[26] Scandella BP, Varadharajan C, Hemond HF, et al. A conduit dilation model of methane venting from lake sediments. Geophys Res Lett 2011;38(6):L06408.
[27] Wu JY, Ning FL, Trinh TT, et al. Mechanical instability of monocrystalline and polycrystalline methane hydrates. Nat Commun 2015;6:8743.
[28] Hembram BK, Mahmud M, Tripathi R, et al. Insights of molecular dynamics simulation to investigate the impact of ethylene glycol on methane hydrate dissociation. Energy Fuels 2024;38(3):1923–33.
[29] Polak E, Ribiere G. Note sur la convergence de méthodes de directions conjuguées. ESAIM: Math Model Num 1969;3(R1):35–43.
[30] Chuvilin EM, Istomin VA, Safonov SS. Residual nonclathrated water in sediments in equilibrium with gas hydrate comparison with unfrozen water. Cold Reg Sci Technol 2011;68:68–73.
[31] Dzyaloshinskii IE, Lifshitz EM, Pitaevskii LP. The general theory of van der Waals forces. Adv Phys 1961;10:165–209.
[32] Yin ZY, Moridis G, Tan HK, et al. Numerical analysis of experimental studies of methane hydrate formation in a sandy porous medium. Appl Energ 2018;220:681–704.
[33] Wu NY, Liu LH. Review of marine gas hydrate research in China. Edinburgh, Scotland: United Kingdom; 2011.
[34] Boswell R, Yamamoto K, Tamaki M, et al. New insights into the occurrence and implications of mobile water in gas hydrate systems. Energy Fuels 2022;36:2447–61.
[35] Hong WL, Pape T, Schmidt C, et al. Interactions between deep formation fluid and gas hydrate dynamics inferred from pore fluid geochemistry at active pockmarks of the Vestnesa Ridge, west Svalbard margin. Mar Petrol Geol 2021;127:104957.
[36] Kondori J, Zendehboudi S, James L. New insights into methane hydrate dissociation: Utilization of molecular dynamics strategy. Fuel 2019;249:264–76.
[37] Wang J, Hou QL, Zeng FG, et al. Stress sensitivity for the occurrence of coalbed gas outbursts: a reactive force field molecular dynamics study. Energy Fuels 2021;35:5801–7.
[38] Wang J, Hou QL, Zeng FG, et al. Gas generation mechanisms of bituminous coal under shear stress based on ReaxFF molecular dynamics simulation. Fuel 2021;298:120240.
[39] Wei L, Malinverno A, Colwell F, et al. Reactive transport modeling of organic carbon degradation in marine methane hydrate systems. Sci Rep-UK 2024;14:2837.
[40] Li W, Fang B, Tao ZT, et al. Probing the instability of surface structure on solid Hydrates: a microscopic perspective through experiment and simulation. Appl Surf Sci 2024;648:158971.
[41] Canale L, Comtet J, Niguès A, et al. Nanorheology of interfacial water during ice gliding. Phys Rev X 2019;9:041025.
[42] Xiao P, Li JJ, Chen W, et al. Enhanced formation of methane hydrate from active ice with high gas uptake. Nat Commun 2023;14:8068.
[43] He Z, Linga P, Jiang J. What are the key factors governing the nucleation of CO_2 hydrate? Phys Chem Chem Phys 2017;19:15657–61.
[44] Jang J, Santamarina J. Fines classification based on sensitivity to pore-fluid chemistry. J Geotech Geoenviron Eng 2016;142:06015018.
[45] Lei L, Santamarina J. Laboratory strategies for hydrate formation in fine-grained sediments. J Geophys Res-Sol Ea 2018;123:2583–96.
[46] Linga P. Impact of mobile water on energy production from methane hydrates. Energy Fuels 2022;36:2305.